

PHOTONICS Research

Blind zone-suppressed hybrid beam steering for solid-state Lidar

CHAO LI,  XIANYI CAO, KAN WU,* GAOFENG QIU, MINGLU CAI, GUANGJIN ZHANG, XINWAN LI, AND JIANPING CHEN

State Key Laboratory of Advanced Optical Communication Systems and Networks, Department of Electronic Engineering, Shanghai Jiao Tong University, Shanghai 200240, China

*Corresponding author: kanwu@sjtu.edu.cn

Received 9 March 2021; revised 23 June 2021; accepted 29 June 2021; posted 1 July 2021 (Doc. ID 424393); published 1 September 2021

We demonstrate a blind zone-suppressed and flash-emitting solid-state Lidar based on lens-assisted beam-steering technology. As a proof-of-concept demonstration, with the design of a subwavelength-gap 1D long-emitter array and multiwavelength flash beam emitting, the device was measured to have 5% blind zone suppression, $0.06^\circ/\text{point}$ -deflection step, and $4.2\ \mu\text{s}$ scanning speed. In time-of-flight ranging experiments, Lidar systems have a field of view of $11.3^\circ \times 8.1^\circ$ (normal device) or $0.9^\circ \times 8.1^\circ$ (blind-zone suppressed device), far-field number of resolved points of 192, and a detection distance of 10 m. This work demonstrates the possibility that a new integrated beam-steering technology can be implemented in a Lidar without sacrificing other performance. © 2021 Chinese Laser Press

<https://doi.org/10.1364/PRJ.424393>

1. INTRODUCTION

Light detection and ranging (Lidar) technologies have been widely applied in autonomous driving, sensing, wind detection, etc. In recent years, all solid-state Lidar systems have attracted wide attention for their high potential to achieve revolutionary performance. The key point is to replace the bulky mechanical beam-steering components with solid-state nonmechanical beam-steering components. Various nonmechanical beam-steering technologies have been proposed, including lens-assisted beam steering (LABS) [1–10], optical phased array (OPA) [11–22], micro-electro-mechanical systems (MEMS) mirror [23–25], liquid crystal [26,27], etc. However, fundamental limits emerge when they solve the problem of nonmechanical beam steering. For example, OPA-based beam steering has relatively high control complexity, requirement of precise analog control, and limited sidelobe/background suppression. MEMS mirror-based beam steering has a limited steering speed as well as the potential problem of mechanical fatigue. In recent years, LABS has attracted increasing attention for its advantages of very low control complexity and high sidelobe/background suppression. It consists of a $1 \times N$ switch, N emitters connected to N outputs of the switch, and a lens. The light beam is guided to one of the emitters through the switch and emitted to the free space. Then, the lens collimates the beam and steers its direction. If the $1 \times N$ switch is realized by a binary tree structure of 1×2 switches, only $\log_2 N \times 1 \times 2$ switches work simultaneously, corresponding to a control complexity and power consumption of $O(\log_2 N)$. Meanwhile, because only

one emitter emits a light beam in any time, a sidelobe/background suppression of more than 20 dB can be easily obtained.

Various LABS devices have been explored with different features, including ring switches [5], integrated planar lens [1,3], binary switch tree [6,9], metalens [4], photonic crystal waveguide (PCW) grating [2,8,28,29], MEMS emitter [10], and MEMS optical switch [7]. However, limitations also exist in LABS technology such as blind zone and steering speed, which come from the beam-steering principle and limited performance of basic components, e.g., lens, emitter, optical switch.

The existence of a blind zone in the field of view (FOV) results from the principle of discrete beam steering in LABS devices. As the far-field FOV is exactly the image of the beam pattern on the emitter plane, any gap between two emitters will lead to a blind zone in the FOV. Therefore, a blind zone can be suppressed by increasing the fill factor of the emitter array, i.e., the emitters should be placed as densely as possible. For the 2D emitter array, the emitter fill factor is limited by switch size, waveguide-bending radius, and/or emitter size. In a few reported architectures with either a 2D ring emitter array [4], MEMS emitter array [10], or normal grating emitter array [5–7], the fill factors are typically only 5% or less. A hybrid architecture with a 1D long emitter array and wavelength tuning can improve the fill factor, as the emitters can be placed close to each other. A 1D PCW grating array [2,8,28,29] has been proposed to enhance the angular dispersion for wavelength-assisted beam steering as well as to improve the fill factor. But the propagation loss of PCW is higher than that of a strip waveguide.

The steering speed of LABS device is another issue, as it determines the target detection speed in Lidar applications. The widely used thermo-optic switches [1–6,8,9,30] typically have tens of μs switching speed, which is slow. Electro-optic switches in silicon [31,32] can achieve nanosecond-level speed but have higher loss and are less capable of handling high optical power. MEMS-based switches [7,10] have a few microseconds speed but can be vulnerable to vibration and mechanical fatigue. Therefore, a more advanced Lidar design must be employed to overcome the speed limitation in LABS technology.

In this work, we demonstrate a hybrid LABS-based Lidar system that overcomes the fundamental limits in LABS. First, an off-chip cylindrical lens is set on a switchable 1D long-emitter array to obtain high beam quality. Then, with a novel Lidar structure that implements a parallel flash beam emitting and subwavelength-gap 1D long-emitter array, the blind zone, one fundamental limit of LABS, is significantly reduced to 5%, corresponding to a deflection angle resolution of $0.06^\circ/\text{point}$. Moreover, the detection speed, another fundamental limit, can be multiplied by the number of parallel channels. In the proof-of-concept experiment, the Lidar works under time-of-light ranging mode with 16×12 point beam steering, $11.3^\circ \times 8.1^\circ$ FOV, and 25 dB background suppression. A blind-zone suppressed LABS Lidar with an FOV of $0.9^\circ \times 8.1^\circ$ is also implemented for ranging experiments. This work demonstrates that the fundamental limits of LABS can be overcome with proper Lidar design without sacrificing other performance, which would be a solid step toward a truly practical all-solid-state Lidar for various applications, including autonomous driving, 3D imaging, etc.

2. PRINCIPLE OF 2D BEAM STEERING

To overcome the fundamental limits of blind zone and limited beam-steering speed, a wavelength-assisted LABS design is employed, as shown in Fig. 1. The device consists of an on-chip 1×16 switch with thermal control, a 1D emitter array with a staircase structure, and an off-chip cylindrical lens. The light source is coupled into the chip by a standard lensed fiber. The silicon-nitride waveguide was designed with a size of

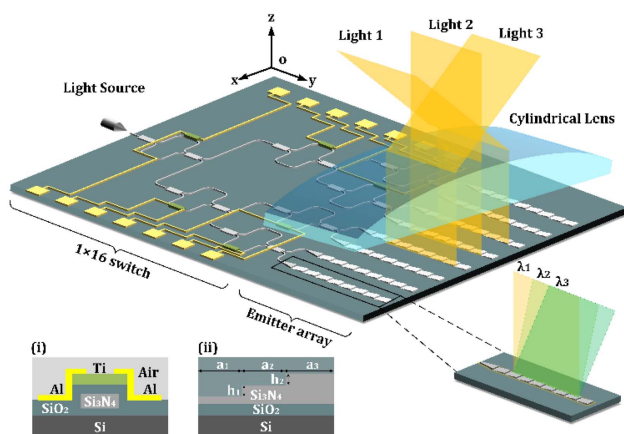


Fig. 1. Schematic illustration of cylindrical lens-based beam-steering device. Inset: Cross-section of (i) thermal switch and (ii) staircase grating.

$1 \mu\text{m} \times 0.4 \mu\text{m}$ to support TE/TM mode operation near 1550 nm. The 1×16 switch is realized by a binary tree of cascaded 1×2 Mach-Zehnder interferometer (MZI) switches with thermal control, where the heating resistors are titanium film deposited on silica cladding, and the wiring lines and bonding pads are aluminum. A cross section of the switch is depicted in inset (i) of Fig. 1. The 1D emitter array consists of 16 grating emitters, which are connected by 16 outputs of the switch. The grating emitter was designed to have a staircase structure with three stages, as shown in inset (ii) of Fig. 1. Above the chip, an off-chip cylindrical lens is set, and its focal plane is overlapped with the plane of an emitter array. Light emitted from a certain grating is collimated and steered in the xoz plane. In the $yo z$ plane, the emission angle of light is controlled by the wavelength of the light source and not affected by the cylindrical lens.

The beam-steering principle in two dimensions is further illustrated in Fig. 2. A circular lens denoted as “FT lens” is set in the setup to perform the Fourier transform and obtain the far-field beam pattern of the light emitted from the system. The FT lens has the same focal length as the cylindrical lens. In the xoz plane, as shown in Fig. 2(a), beam steering is based on LABS technology. Light beams emitted from different grating emitters are collimated and steered by the cylindrical lens. It should be emphasized that these light beams do not exist at the same time because each time only one grating emitter is turned on to emit light. However, these light beams virtually intersect at one point (denoted as “S”) on the focal plane of the cylindrical lens on the other side. This means by switching light to emit from different emitters, different directions of beam steering in the far field can be achieved. The beam divergence $\Delta\theta_{xoz}$ and FOV θ_{xoz} in the xoz plane are given by [6]

$$\Delta\theta_{xoz} = \arctan\left(\frac{w}{f}\right), \quad (1)$$

$$\theta_{xoz} = 2 \arctan\left(\frac{l}{2f}\right), \quad (2)$$

where w is the near-field beam diameter, l is the size of the emitter array, and f is the focal length of two lenses. The beam steering step θ'_{xoz} can be expressed as

$$\theta'_{xoz} \approx \arctan\left(\frac{p}{f}\right) \approx \frac{\theta_{xoz}}{N-1}, \quad (3)$$

where p is the distance between two adjacent emitters, and N is the number of emitters. As each emitter corresponds to a beam direction in the far field, N emitters correspond to N different beam directions; thus, the number of resolved points in the far field is N . In the $yo z$ plane, as depicted in Fig. 2(b), light beams of different wavelengths emitted from the same grating are

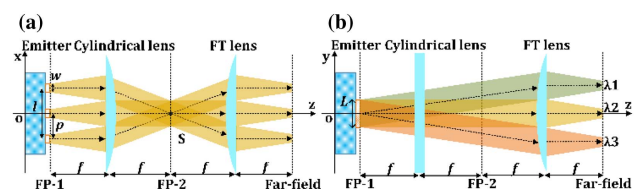


Fig. 2. Principle of beam steering in (a) xoz plane and (b) $yo z$ plane.

Table 1. Performance Comparison of Hybrid LABS Devices

Reference	Structure	Beam Quality	Blind Zone	Main Loss (Value)	Scanning Method
[1]	Planar lens + 1D grating	Aberration	>50%	a-Si lens (NA)	Thermo-optic switch + wavelength tuning
[8]	Prism lens + 1D PCW grating	NA	87.5%	PCW (10–30 dB/cm)	Thermo-optic switch + wavelength tuning
Our work	Cylindrical lens + 1D grating	25 dB background suppression	5%	Grating (1–3 dB/cm)	Thermo-optic switch + flash emitting

diffracted into different directions according to the grating diffraction equation given by [33]

$$\Phi = \arcsin\left(\frac{\beta}{k_0} - \frac{\lambda}{\Lambda}\right), \quad (4)$$

where Φ is the diffraction angle, λ is the wavelength, β is the propagation constant of light mode in the grating, k_0 is the wavenumber in vacuum, and Λ is the grating period. The FOV angle φ_{yoz} can be derived by differentiating Eq. (4) with respect to λ as [28]

$$\varphi_{yoz} = -\frac{n_g - n_r}{\lambda \sqrt{1 - n_r^2}} \Delta\lambda, \quad (5)$$

where $n_g = -(\lambda^2/2\pi) \cdot (d\beta/d\lambda)$ is the group index, $n_r = \beta/k_0 - \lambda/\Lambda$ is the modal equivalent index of the radiated light, and $\Delta\lambda$ is the wavelength range of input light. The beam divergence $\Delta\varphi_{yoz}$ is expressed as follows based on the Fraunhofer diffraction theory [33]:

$$\Delta\varphi_{yoz} = \frac{0.886 \times \lambda}{L}, \quad (6)$$

where L is the effective grating length when light power decreases to $1/e$. The divergence and emitting angles remain unchanged in the yoz plane when light beams propagate through the cylindrical lens. Similarly, the far-field beam pattern in the yoz plane is then obtained by the FT lens. According to Eqs. (4)–(6), both beam divergence and diffraction angle in the yoz plane depend on the wavelength of light. Further, the FOV in the yoz plane is determined by the wavelength range.

To summarize, beam steering in the xoz plane is determined by the beam pattern on the emitter plane. The blind zone in the far field is generated by the gap between two adjacent grating emitters. Beam steering in the yoz plane is determined by the wavelength tuning, which is gapless in the far field and does not create a blind zone. Moreover, simultaneously emitting multiple wavelengths (flash beam emitting) can multiply the detection speed by the number of wavelength channels. Although similar hybrid architectures are also proposed in some LABS devices, the reported works all have limited performance in some key specifications. A detailed performance comparison among our work and other hybrid architectures is listed in Table 1. It is clear that our work exhibits a balanced performance in nearly all key specifications.

3. DEVICE CHARACTERIZATION

A. Device Fabrication

The chip was fabricated on a 6 mm × 16 mm silicon-nitride isolator wafer with a silicon photonic CMOS process.

A minimum feature size of 200 nm in the grating structure is achieved by electron beam lithography. Figure 3(a) shows the photograph of the chip. It includes four stages of cascaded 1 × 2 MZI switches and 16 grating emitters placed in parallel. The inset picture in Fig. 3(a) illustrates the radiation beam pattern of the staircase grating captured by an infrared camera (Xenics Bobcat-320). Figure 3(b) shows the setup of our beam-steering device, where a cylindrical lens with a focal length of 10 mm (Thorlabs LJ1878L2-C) is set above the chip. The thermo-optical switch on chip was measured to have a rise time (10%–90%) of ~50 μs, as shown in Fig. 3(c), of which the power consumption and extinction ratio were measured to be ~120 mW/π and ~25 dB.

Generally, the emission efficiency of the Si₃N₄ Bragg grating is limited because of the low refractive index contrast compared with silicon. Methods, including the distributed Bragg reflector [34], staircase structure [35], and dual-level grating structure [36], are proposed to increase the directionality of the Si₃N₄ grating. Among these structures, the staircase grating is demonstrated to support an efficiency of 71% with a single layer

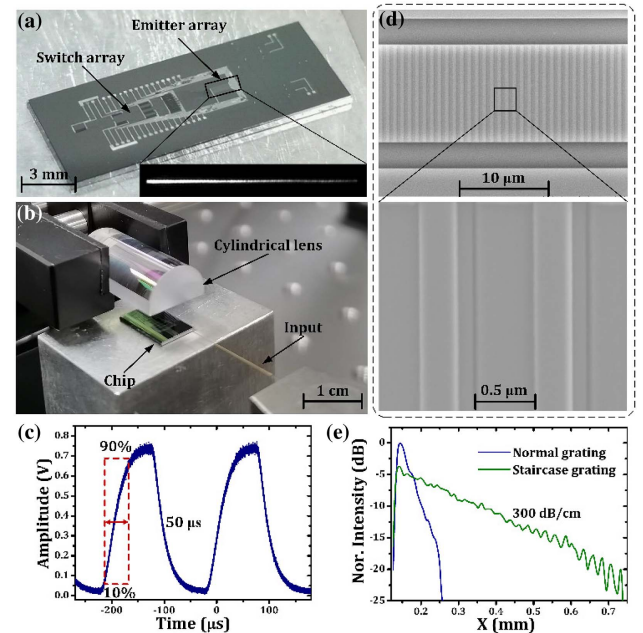


Fig. 3. (a) Photograph of the chip with switch and emitter array. Inset: Radiation intensity of staircase grating captured by an infrared camera. (b) Photograph of the beam-steering device. (c) Speed measurement of the thermo-optical switch. (d) SEM image of the staircase grating. Inset: Zoom-in image. (e) Comparison of radiation intensity between staircase and normal gratings.

structure. Besides, an enhanced upward emission efficiency of 50%–90% can be obtained for a staircase grating with a radiation length of 40 μm in the FDTD simulation, whereas a normal grating with single full-depth etching can only have an efficiency below 50%. The high directionality results from the constructive interference in the upward direction between scattering lights from two consecutive trenches. Therefore, in our device, as shown in Fig. 3(d), the emitters were fabricated as staircase gratings to increase directionality. Considering that a grating with long radiation length is required to obtain small beam divergence in the far field according to Eq. (6), there is a trade-off between the beam divergence angle and emission efficiency during the grating design. A parameter optimization based on particle swarm algorithm is applied in simulation. As shown in the inset of Fig. 3(d), the staircase grating was fabricated with a width of $\sim 11 \mu\text{m}$, a length of $\sim 1 \text{ mm}$, an etching depth of 50 nm, and a period of $\sim 0.96 \mu\text{m}$. The upward emission efficiency is simulated to be 64%. Experimental emission efficiency of a long waveguide grating is obtained by light beam brightness comparison with a standard grating coupler in the infrared image.

As shown in Fig. 3(e), the staircase grating was measured to radiate 23% more power than a normal single-etched grating (50%). It has an attenuation coefficient of 300 dB/cm along the propagation direction and an effective grating length of 145 μm (power decreases to $1/e$). The spacing between two adjacent gratings is designed with two values, i.e., 121 and 0.6 μm . The device with large grating spacing is to achieve a relatively large FOV with limited grating number according to Eq. (2). The device with small grating spacing is to demonstrate that the

blind zone of device with 121 μm spacing can be significantly suppressed according to Eq. (3).

B. Two-Dimensional Beam Steering

The two-dimensional nonmechanical beam steering in our device is achieved by guiding the light to be emitted from a certain emitter in the array and tuning the input wavelength. In the experiment, a wavelength-tunable continuous wave laser is coupled into the chip through a lensed fiber for wavelength-assisted beam steering demonstration. The light is routed into one of the 16 emitters by the cascaded 1×2 MZI switches on the chip. Above the chip, a cylindrical lens is utilized to collimate and steer the up-emitting light in the yoz plane, as described in Section 2.

We first characterize the grating emission properties by removing the cylindrical lens and placing a Fourier transform lens (FT lens, a circular plano-convex lens with 10 mm focal length), as shown in Fig. 4(a). The output of the FT lens is captured by an infrared camera with a detection dynamic range of 0–65,535. As shown in Fig. 4(b), the measured far-field grating emission pattern exhibits a wide divergence angle ($\sim 8.9^\circ$) along the θ direction due to the narrow grating width and a narrow divergence angle ($\sim 0.5^\circ$) along the φ direction due to the long grating length. When the wavelength changes from 1455 to 1565 nm, the emission angle shifts $\sim 8.1^\circ$ along the φ direction. In Fig. 4(b), a few typical measured patterns with different input wavelengths are plotted together for a clear view. Then, the cylindrical lens is placed together with the FT lens for the far-field measurement of the beam-steering device (grating spacing of 121 μm), as shown in Fig. 4(c). Similarly, all the

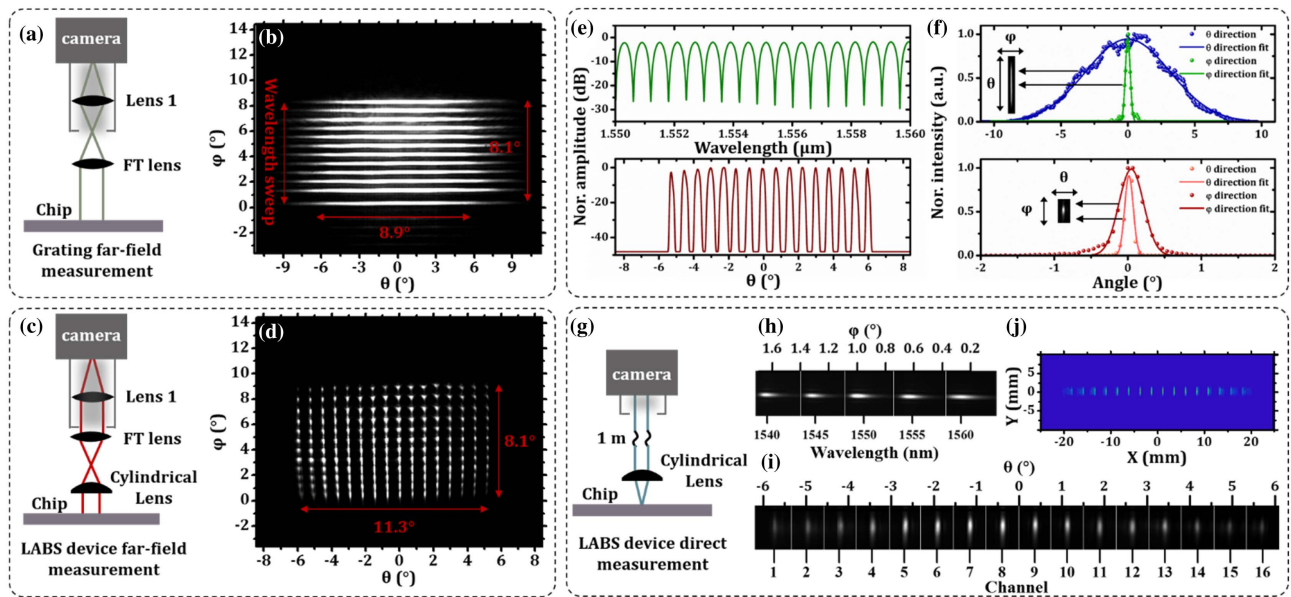


Fig. 4. (a) Experimental setup for far-field measurement of grating. (b) Far-field beam pattern of grating with wavelength range of 110 nm. (c) Experimental setup for far-field measurement of LABS device. (d) Far-field beam-steering pattern by emitter selecting and wavelength tuning. (e) Typical transmission spectrum of a 1×2 MZI switch with unequal arms (upper panel) and cross-sectional powers of beam pattern along θ direction at 1550 nm (lower panel). (f) Cross-sectional powers and fitted results of far-field beam pattern from grating (upper panel) and LABS device (lower panel). Inset: Single beam patterns from (b) and (d). (g) Experimental setup for direct measurement of far-field beam patterns from LABS device. (h) Beam-steering patterns by wavelength tuning. (i) Beam-steering patterns by LABS. (j) Beam-steering patterns by LABS in Zemax simulation.

measured far-field patterns are plotted together in Fig. 4(d) for a clear view. The FOV is $\sim 11.3^\circ$ along the θ direction based on LABS and $\sim 8.1^\circ$ along the φ direction based on wavelength tuning. This confirms the property that the addition of the cylindrical lens does not affect the beam-steering angle based on wavelength tuning. A nearly linear relation of $\sim 0.07^\circ/\text{nm}$ between wavelength and grating emission angle (φ) is obtained in simulation and experiment. Based on the LABS principle, there is only one grating emitting light each time, and the background noise is dominated by the leaked power from unworking emitters through nonideal switches. Therefore, the background suppression is determined by the extinction ratio of switches [upper panel of Fig. 4(e)], which is 25 dB. Except for the power leakage from other emitters, more than 40 dB background suppression can be realized, as depicted in the lower panel of Fig. 4(e), which is the cross-sectional power of beam patterns along the θ direction with $\varphi = 7^\circ$ in Fig. 4(d). Moreover, the typical cross-sectional powers of the beam patterns in Figs. 4(b) and 4(d) are shown in Fig. 4(f). It can be seen that, after the collimation of cylindrical lens, the divergence of the light beam from the grating has been compressed from $8.9^\circ \times 0.5^\circ$ in the θ and φ directions [Fig. 4(f) upper panel] to $0.1^\circ \times 0.5^\circ$ [Fig. 4(f) lower panel], which is close to the theoretical value of $0.063^\circ \times 0.54^\circ$.

To further confirm the measurement accuracy of the steering angles, we also measured the far-field beam patterns by directly placing the infrared camera 1 m away from the device, as shown in Fig. 4(g). Different far-field angles were measured by moving the camera. The results are shown in Figs. 4(h) and 4(i) from wavelength tuning and LABS, respectively. Similarly, all the measured beam patterns are plotted together in the figures. The steering angle is $\pm 5.65^\circ$ for LABS in the θ direction and 1.47° for wavelength tuning (1540–1560 nm) in the φ direction. Both agree well with the measurement results based on the FT lens. There is an intensity reduction of the beam pattern from the center emitter to edge emitter, which is a result of aberration from the cylindrical lens. The same result is confirmed by simulation, as shown in Fig. 4(j). Generally, it can be improved by utilizing a better lens system.

C. Blind Zone Suppression

As explained in Section 2, a 1D long-emitter array in our design allows densely placed grating emitters, and the gap between adjacent gratings can be significantly reduced, corresponding to a highly suppressed blind zone in the far field. Our previous work shows a blind zone suppression with defocusing method, but the cost is the increase of beam divergence [6]. To achieve a small gap, one needs to reduce the crosstalk between two adjacent grating emitters. In this work, a grating with a large core area is designed so that the light beam can be well confined in the waveguide. For a cross section of $11 \text{ mm} \times 0.4 \text{ }\mu\text{m}$ and a grating length of 2.5 mm, Fig. 5 shows the experimental and simulated crosstalk with different grating gaps. Crosstalk between two adjacent gratings is simulated to be -60 and -30 dB with gaps of 1.5 and $0.6 \text{ }\mu\text{m}$. Experimental measurement of crosstalk between gratings has also been implemented. We fabricated two waveguide grating emitter arrays with emitter gaps of 1.5 and $0.6 \text{ }\mu\text{m}$ and an adequate coupling length of 2.5 mm. When light is guided into one grating of the emitter array, the

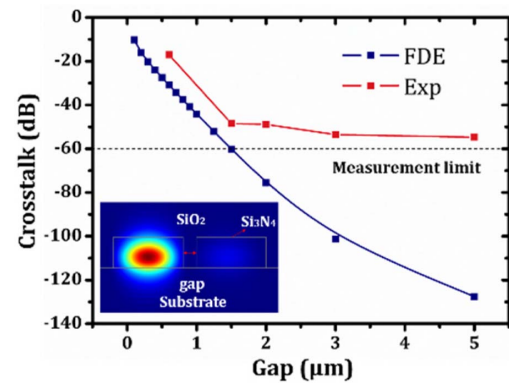


Fig. 5. Crosstalk between two grating emitters with different gaps. Inset: Simulated mode distribution from a finite-difference-eigenmode (FDE) solver.

crosstalk is -48 and -17 dB, respectively. The micrographs are shown in Figs. 6(a) and 6(b), respectively. Besides, further evidence such as dark lines between beam patterns can be observed in the zoomed-in images of two types of emitter arrays when all the gratings are lit up, as displayed in Figs. 6(c) and 6(d).

Further demonstration of blind-zone-suppressed beam steering is carried on in our device with a $0.6 \text{ }\mu\text{m}$ gap waveguide grating emitter array. We have obtained a far-field FOV of 0.91° based on LABS and an FOV of 8.1° based on wavelength tuning in our device, as depicted in Fig. 7(a). Both vertical and horizontal beam steerings are shown individually in Figs. 7(b) and 7(c) for a clear observation. It has a same FOV by wavelength tuning, as we have proved in Figs. 4(a) and 4(b), but a higher resolution point by LABS in the same FOV. For example, there are only two points in an FOV of 0.91° in a $121 \text{ }\mu\text{m}$ gap grating array, and 16 points in the same FOV in a $0.6 \text{ }\mu\text{m}$ gap grating array, and the minimum deflection angle has been decreased from $0.75^\circ/\text{point}$ to $0.06^\circ/\text{point}$. As shown in Fig. 7(c), there is no blind zone observed between two adjacent

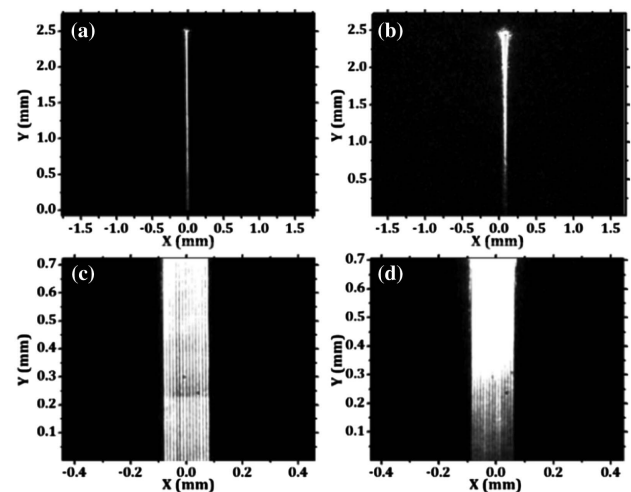


Fig. 6. Near-field beam pattern with one grating lit up in grating emitter array with gaps of (a) $1.5 \text{ }\mu\text{m}$ and (b) $0.6 \text{ }\mu\text{m}$. Near-field beam pattern with all gratings lit up with gaps of (c) $1.5 \text{ }\mu\text{m}$ and (d) $0.6 \text{ }\mu\text{m}$.

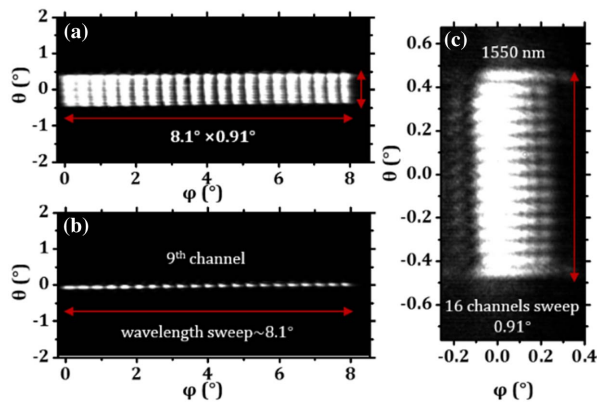


Fig. 7. Far-field beam-steering pattern realized by (a) 16-channel 0.6 μm gap emitters selecting and wavelength tuning, (b) wavelength sweep, and (c) 16-channel emitters selecting.

channels of the beam pattern. Though the FOV of a device with 0.6 μm gap grating array decreased under the same number of emitters, it can be enhanced to 11.3° by fabricating 170 close-packed waveguide gratings.

If we define a parameter “blind zone suppression (BZS)” as the ratio between the total emission beam area and the total area occupied by the emitters, our design supports a BZS of 88% $[= 11 \mu\text{m}/(11 + 1.5) \mu\text{m}]$ and a maximum BZS of 95% $[= 11 \mu\text{m}/(11 + 0.6) \mu\text{m}]$ in experiment; that is, the blind zone only occupies 5% of the FOV. Other reported LABS Lidar systems all have a blind zone more than 50% (see Section 5).

4. LIDAR DEMONSTRATION

The Lidar that overcomes the fundamental limits of LABS is then demonstrated, as shown in Fig. 8. The ranging technology is time-of-light (TOF) ranging. A femtosecond pulsed laser with a broadband spectrum near 1550 nm is utilized as the light source. After the laser, a pulse picker is applied to reduce the laser repetition rate from 37 MHz to 20 kHz. Then, a spectral filter is introduced to select the desired spectrum as different wavelength channels. The schematic illustrations of the corresponding spectra and waveforms are shown as insets (i)–(iii) in

Fig. 8. The preprocessed pulsed light source is divided into two paths: 10% of it is guided to a photodetector, as timing 90% of it is amplified by an erbium-doped fiber amplifier, controlled by a polarization controller (PC), and coupled into the chip via a lensed fiber. On the chip, the light is guided to one certain grating emitter by the 1×16 switch and emitted to the free space. The pulses with different wavelengths overlap in the time domain. Thus, they simultaneously are emitted to different directions from the grating emitter (flash beam emitting). After collimation of the cylindrical lens, the collimated beams simultaneously detect the target along φ direction (wavelength dependent direction). The beams are then scanned along the θ direction (LABS direction) by switching the light to different grating emitters on the chip. The reflected beams are collected by a receiver consisted of a lens, a fiber array, and a few avalanche photodiodes (APDs). In principle, fibers receiving the reflected beams along the θ direction (LABS direction) do not work at the same time, so their output can be detected by a same APD. Therefore, the required number of APDs is equal to the number of wavelength channels. In the future, a 1D APD array can be used. The electrical signal output by the APDs together with the reference signal is finally processed to obtain the timing difference and target distance. A photograph of the experimental setup is shown in Fig. 9.

The advantage of such a Lidar design is that it fully exploits the low control complexity and clean beam emission of LABS while overcoming its fundamental limits of blind zone and relatively low speed. The blind zone is eliminated in the y direction by wavelength tuning and suppressed in the x direction by reducing the gap between emitters. The speed is improved by flash beam emitting. That is, all the light pulses with different wavelengths are emitted simultaneously. Such a parallel detection multiplies the detection speed per pixel by the number of wavelength channels. The experimentally measured spectra and time-domain waveforms of the preprocessed light source are shown in Figs. 10(a) and 10(b). In this proof-of-concept demonstration, 12 wavelength channels from 1544 to 1562 nm are selected. The channel spacing is 1.6 nm, corresponding to an emission angle difference of 0.1° . The repetition rate is 20 kHz. The pulse duration is ~ 500 ps. The loss of our chip is about -12 dB, including -4 dB of fiber-to-chip coupling loss, -6 dB of 1×16 switch insertion loss (1.5 dB each 1×2 MZI

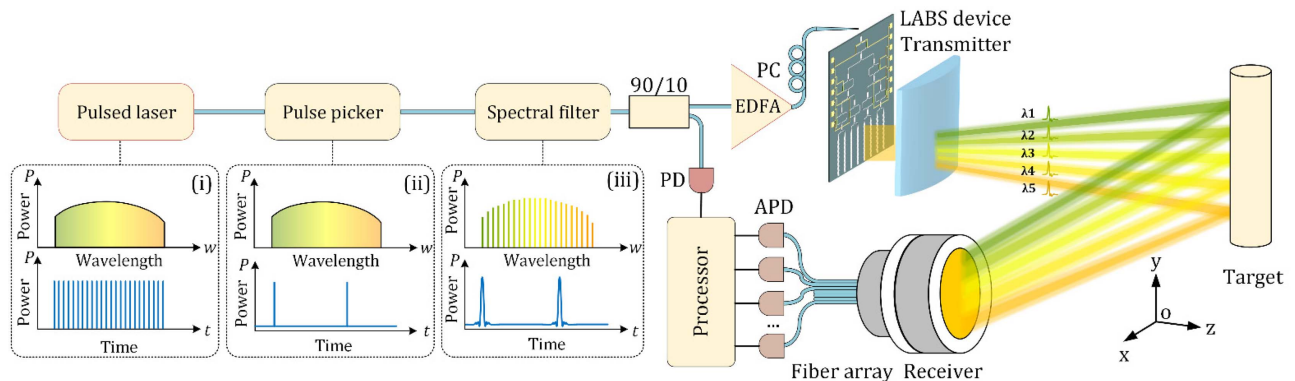


Fig. 8. Experimental setup of target detection with the beam-steering device. Inset: Output spectra and waveforms of (i) pulsed laser, (ii) pulse picker, and (iii) spectral filter.

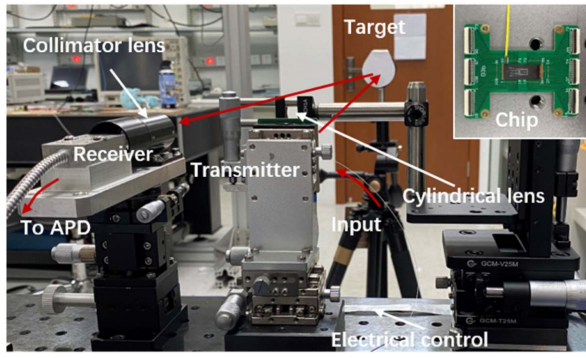


Fig. 9. Picture of experimental setup of Lidar. Inset: Picture of LABS chip with electrical control.

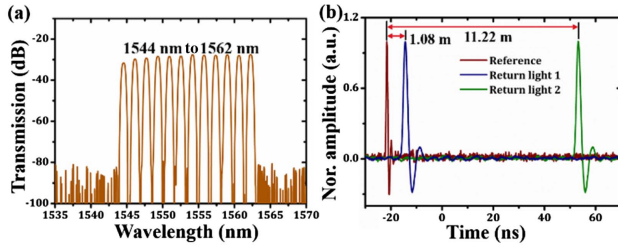


Fig. 10. (a) Optical spectrum of the light source. (b) Waveforms of reference signal and two returning signals scattered by the targets at 1.08 and 11.22 m.

switch), and -2 dB of grating emission loss. The average output power of our device is measured to be -30.51 dBm. The target is a white A4 paper. The power of returning light P_r can be expressed as [9]

$$P_r = \frac{P_t A_r^2 r_t t_a}{8R^2}, \quad (7)$$

where P_t is the power of emitted light from the transmitter, A_r is the receiver aperture, r_t is the reflectivity of target, t_a is the air transmission, and R is the target distance. The receiver lens has a diameter of 2.05 cm, and an amplified APD with a response bandwidth of 200 MHz is used. The target distance can be obtained by calculating the time delay between the received signal and the reference signal. Figure 10(b) shows two typical returning signals at a distance of 1.08 and 11.22 m, respectively. The loss related to the beam propagation and target diffuse reflection is estimated to be ~50 dB according to Eq. (7). The target at 11.22 m is a highly reflective mirror for proof-of-concept demonstration.

To evaluate the ranging accuracy, three groups of ranging experiments by LABS (measurements 1, 2) and wavelength tuning (measurement 3) are performed. Targets are placed with a separation of 15 cm within a range of 3 m in the horizontal direction (LABS direction) and a separation of 20 cm within a range of 1.5 m in the vertical direction (wavelength direction), respectively. The corresponding waveforms of the returning signals are provided in Fig. 11. The comparison of measurement results between TOF ranging and manual measurement is shown in Fig. 12(a). The maximum deviation is 0.35 ns corresponding to 5 cm ranging difference, which is mainly due to

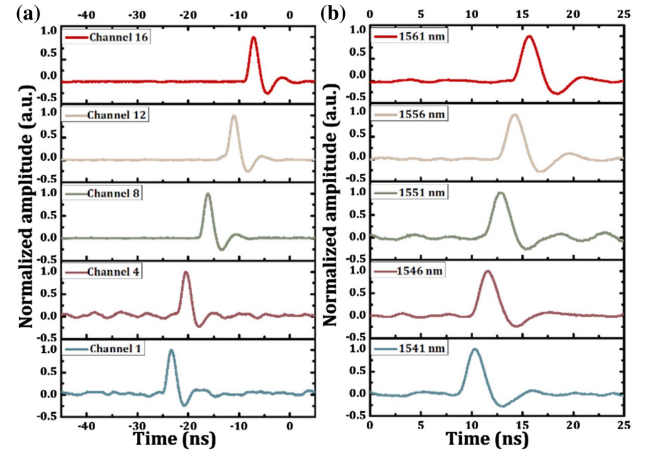


Fig. 11. Waveforms of returning signals from different directions along (a) emitter channels of 1, 4, 8, 12, and 16 and (b) wavelength channels from 1541 to 1561 nm.

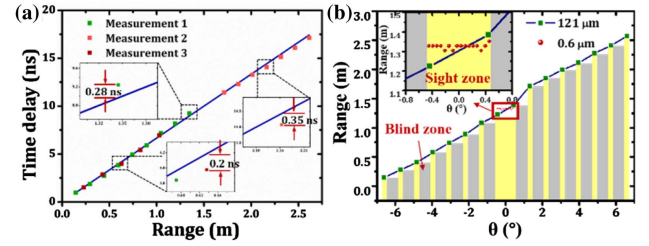


Fig. 12. (a) Time delays of returning pulses with respect to target distance in three measurements from eighth emitter channel at 1550 nm. (b) Ranging results comparison between beam-steering devices with 121 and 0.6 μm spacing grating array. Inset: Zoomed view of ranging results of the device with 0.6 μm spacing grating array.

the manual measurement error. The theoretical ranging error ΔR of TOF lidar is given by [9]

$$\Delta R = 0.5 \left(\frac{\tau_r}{\text{SNR}} \right) c, \quad (8)$$

where τ_r is the pulse rise time, SNR is the signal-to-noise ratio of the returning signal, and c is the speed of light in vacuum. For our system, the pulse rise time is 0.825 ns limited by the bandwidth of amplified APD (200 MHz), and the SNR of the returning signal is ~46.7. Therefore, the ranging error is calculated to be ~2.65 mm.

Additionally, a proof-of-concept demonstration of blind-zone suppression in a Lidar system has been performed. The results of a comparison experiment of ranging along the emitter direction between devices with 121 μm spacing grating array and 0.6 μm spacing grating array are shown in Fig. 12(b). Though the beam-steering device with 121 μm spacing gratings has an FOV of 11.3°, the targets can be detected only when they locate in the yellow region (sight zone) in Fig. 12(b), which corresponds to a blind zone of 91.7%. However, the blind zone can be suppressed to 5% by the device with 0.6 μm spacing grating array, as depicted in the inset of Fig. 12(b). Besides, as discussed in Section 3.C, the FOV can be simply

increased by increasing the number of gratings with large-scale integration.

5. DISCUSSION

A. Performance Comparison

Until now, although such beam-steering technologies have been proposed, only a few Lidar demonstrations based on these new technologies [9,10,30,37–41] have been reported. One reason could be that the above-mentioned fundamental limits have become the biggest obstacles that prevent novel nonmechanical beam-steering technologies from practical Lidar application. A performance comparison among our work and other solid-state Lidar systems based on integrated OPA and LABS has been performed, as shown in Table 2. It can be clearly observed that only our Lidar design can support a BZS up to 95%, whereas other LABS-based Lidars typically have a BZS below 50%. That is, more than half of the FOV cannot be detected. Moreover, a flash beam emitting design effectively counterbalances the relatively slow thermo-optic (TO) switching speed in silicon nitride. The average detection speed per pixel is $50 \mu\text{s}/12 = 4.2 \mu\text{s}$, where 12 is the number of wavelength channels. Obviously, the detection speed per pixel can be further reduced if more wavelength channels are employed. Compared with OPA-based Lidar, LABS has lower control complexity with $O(\log_2 N)$ complexity, digital control, and better background suppression.

B. FMCW Lidar Demonstration

Recently, a growing interest in frequency-modulated continuous-wave (FMCW) ranging based on coherent detection has emerged. It is demonstrated with high sensitivity and velocity-detection capability. We have also demonstrated that our LABS device can be applied in FMCW Lidar applications, as shown in Fig. 13. The light source is a distributed feedback (DFB) laser with continuous wave output. By applying a saw-like driving current to the DFB laser, a frequency-sweeping light source with a sweeping slope of 23.3 GHz/ms is realized. The sweeping light is then split into two paths; 90% of its power is amplified by an EDFA and injected into the LABS chip. The average output power is estimated to be -9.38 dBm ;

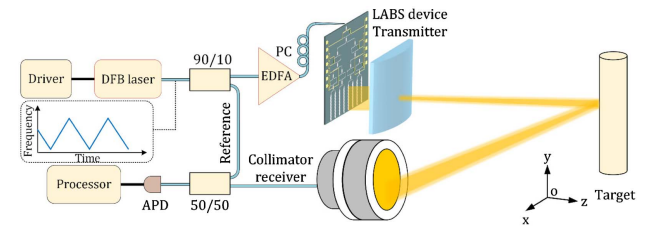


Fig. 13. Experiment setup of FMCW Lidar system based on LABS.

10% of its power is coupled to an avalanche photodetector (APD) as a local reference, together with the returning signals reflected by the target. The transmitter part is unchanged, i.e., the chip with a cylindrical lens. The receiver part is a collimation lens with a coupling fiber. Therefore, the direction of this collimation lens should be adjusted according to the beam direction in the transmitter part. As the wavelength of the DFB laser is fixed, this setup currently only supports 1D scanning along LABS direction. However, an FMCW Lidar based on a microcomb with multiple wavelengths has been recently reported [42]. With such a microcomb, our setup can achieve 2D detection.

Three typical beating signals of the returning signals from 0.3, 0.6, and 1 m are shown in Figs. 14(a)–14(c). The corresponding electrical spectra are shown in Fig. 14(d). Three beating frequencies at 341, 388, and 440 kHz can be clearly observed, which correspond to an approximately linear separation in range, as shown in Fig. 14(e).

C. Future Improvement of Device Performance

To further improve the performance of the LABS chip and Lidar system, a few factors can be considered. The first is the grating emitter. Current two-time etching for the staircase grating increases fabrication errors, complexity, and cost. A substitute method of slanted grating can be introduced to obtain a high emission efficiency as well as low fabrication complexity [43]. The second is the insertion loss of the on-chip devices. It has been reported that the propagation loss in a silicon-nitride waveguide can be as low as $\sim 1 \text{ dB/m}$ with a novel reflow

Table 2. Performance Comparison of Solid-State Lidars with Different Beam Steering and Ranging Technologies

Reference	Beam Steering Tech.	Ranging Tech.	Theoretical Max BZS	Speed ($\mu\text{s}/\text{point}$)	Material	Control Complexity	FOV	Dimension	Resolution
[37]	OPA with TO phase shifters	FMCW	—	30	Si	$O(N)$ analog control	$56^\circ \times 15^\circ$	2D	200
[30]	LABS with TO switches	FMCW	$\sim 50\%$ only for 1D	NA	Si	$O(\log_2 N)$ digital control	70°	1D	8
[10]	LABS with MEMS switches/emitters	TOF	$<10\%$	4	SiN + Si	$O(1)$ digital control	$1^\circ \times 1^\circ$	2D	100
[9]	LABS with TO switches	TOF	$\sim 50\%$	1000	SiO ₂	$O(\log_2 N)$ digital control	$1^\circ \times 1^\circ$	2D	16
This work	LABS with TO switches	TOF	$\sim 95\%/8.3\%^a$	4.2	SiN	$O(\log_2 N)$ digital control	$0.91^\circ \times 8.1^\circ / 11.3^\circ \times 8.1^\circ{}^a$	2D	192

^aThe first and second numbers are from the devices with 0.6 and 121 μm grating spacing, respectively.

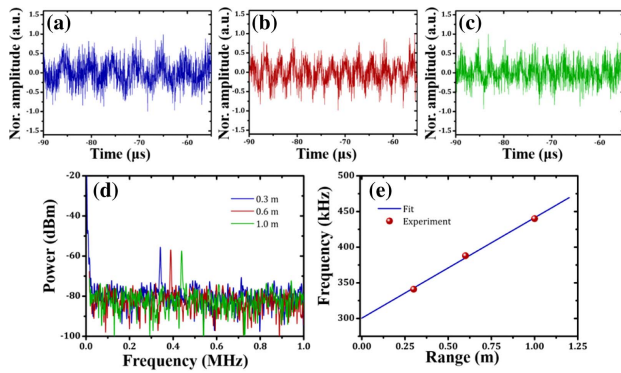


Fig. 14. Waveforms of beating signal from targets of (a) 0.3 m, (b) 0.6 m, and (c) 1 m. (d) Electrical spectra of beating frequencies from three targets. (e) Range of targets with respect to beating frequency.

process [44,45]. Even with standard CMOS technology, the MZI thermo-optic switches can reach an insertion loss of ~ 0.6 dB with leaked power less than -25 dB [46]. Thus, for N -channel output, the total insertion loss can be reduced to $0.6 \cdot \log_2 N$ dB. The last is the coupling loss. With a multi-stage taper design, a fiber-to-chip coupling loss of 0.5 dB can be achieved [47].

6. CONCLUSION

In conclusion, a solid-state TOF Lidar based on hybrid LABS technology is demonstrated on the silicon-nitride platform. The implementation of a 1D long-emitter array and flash beam emitting overcomes the fundamental limits of blind zone and relatively low speed in LABS technology while still maintaining its advantages of low control complexity of $O(\log_2 N)$ and excellent background suppression. This work could be a promising solution for all solid-state-integrated Lidar applications. As a proof-of-concept experiment, we have achieved 16×12 point beam steering and detection in a time-of-flight ranging mode. The emission beam has $0.1^\circ \times 0.5^\circ$ divergence in two orthogonal directions, $11.3^\circ \times 8.1^\circ$ (normal device) or $0.9^\circ \times 8.1^\circ$ (blind-zone suppressed device) FOV and 25 dB background suppression.

Funding. National Natural Science Foundation of China (61875122, 61922056).

Disclosures. The authors declare no conflicts of interest.

Data Availability. No data were generated or analyzed in the presented research.

REFERENCES

- J. J. López, S. A. Skirlo, D. Kharas, J. Sloan, J. Herd, P. Juodawlkis, M. Soljačić, and C. Sorace-Agaskar, "Planar-lens enabled beam steering for chip-scale LIDAR," in *Conference on Lasers and Electro-Optics* (Optical Society of America, 2018), paper SM3I.1.
- H. Abe, M. Takeuchi, G. Takeuchi, H. Ito, T. Yokokawa, K. Kondo, Y. Furukado, and T. Baba, "Two-dimensional beam-steering device

- using a doubly periodic Si photonic-crystal waveguide," *Opt. Express* **26**, 9389–9397 (2018).
- S. Kim, J. Sloan, J. J. López, D. Kharas, J. Herd, S. Bramhavar, P. Juodawlkis, G. Barbastathis, S. Johnson, C. Sorace-Agaskar, and M. Soljačić, "Luneburg lens for wide-angle chip-scale optical beam steering," in *Conference on Lasers and Electro-Optics* (Optical Society of America, 2019), paper SF3N.7.
- Y.-C. Chang, M. C. Shin, C. T. Phare, S. A. Miller, E. Shim, and M. Lipson, "Metalens-enabled low-power solid-state 2D beam steering," in *Conference on Lasers and Electro-Optics* (Optical Society of America, 2019), paper SF3N.5.
- D. Inoue, T. Ichikawa, A. Kawasaki, and T. Yamashita, "Demonstration of a new optical scanner using silicon photonics integrated circuit," *Opt. Express* **27**, 2499–2508 (2019).
- C. Li, X. Cao, K. Wu, X. Li, and J. Chen, "Lens-based integrated 2D beam-steering device with defocusing approach and broadband pulse operation for Lidar application," *Opt. Express* **27**, 32970–32983 (2019).
- X. Zhang, K. Kwon, J. Henriksson, J. Luo, and M. C. Wu, "A 20×20 focal plane switch array for optical beam steering," in *Conference on Lasers and Electro-Optics (CLEO)* (Optical Society of America, 2020), paper SM10.3.
- H. Ito, Y. Kusunoki, J. Maeda, D. Akiyama, N. Kodama, H. Abe, R. Tetsuya, and T. Baba, "Wide beam steering by slow-light waveguide gratings and a prism lens," *Optica* **7**, 47–52 (2020).
- X. Cao, G. Qiu, K. Wu, C. Li, and J. Chen, "Lidar system based on lens assisted integrated beam steering," *Opt. Lett.* **45**, 5816–5819 (2020).
- S. J. Spector, E. H. Cook, M. G. Moebius, F. A. Baruffi, M. G. Bancu, L. D. Benney, S. J. Byrnes, J. P. Chesin, S. J. Geiger, D. A. Goldman, A. E. Hare, B. F. Lane, W. D. Sawyer, and C. R. Bessette, "LiDAR beamsteering by digitally switched MEMS gratings on a silicon photonics platform," in *Conference on Lasers and Electro-Optics* (Optical Society of America, 2020), paper SM10.4.
- J. Sun, E. Timurdogan, A. Yaacobi, E. S. Hosseini, and M. R. Watts, "Large-scale nanophotonic phased array," *Nature* **493**, 195–199 (2013).
- J. Sun, E. S. Hosseini, A. Yaacobi, D. B. Cole, G. Leake, D. Coolbaugh, and M. R. Watts, "Two-dimensional apodized silicon photonic phased arrays," *Opt. Lett.* **39**, 367–370 (2014).
- H. Abediasl and H. Hashemi, "Monolithic optical phased-array transceiver in a standard SOI CMOS process," *Opt. Express* **23**, 6509–6519 (2015).
- D. N. Hutchison, J. Sun, J. K. Doylend, R. Kumar, J. Heck, W. Kim, C. T. Phare, A. Feshali, and H. Rong, "High-resolution aliasing-free optical beam steering," *Optica* **3**, 887–890 (2016).
- T. Komljenovic, R. Helkey, L. Coldren, and J. E. Bowers, "Sparse aperiodic arrays for optical beam forming and LIDAR," *Opt. Express* **25**, 2511–2528 (2017).
- C. V. Poulton, M. J. Byrd, M. Raval, Z. Su, N. Li, E. Timurdogan, D. Coolbaugh, D. Vermeulen, and M. R. Watts, "Large-scale silicon nitride nanophotonic phased arrays at infrared and visible wavelengths," *Opt. Lett.* **42**, 21–24 (2017).
- M. Zadka, Y.-C. Chang, A. Mohanty, C. T. Phare, S. P. Roberts, and M. Lipson, "On-chip platform for a phased array with minimal beam divergence and wide field-of-view," *Opt. Express* **26**, 2528–2534 (2018).
- Y. Zhang, Y.-C. Ling, K. Zhang, C. Gentry, D. Sadighi, G. Whaley, J. Colosimo, P. Suni, and S. J. Ben Yoo, "Sub-wavelength-pitch silicon-photonics optical phased array for large field-of-regard coherent optical beam steering," *Opt. Express* **27**, 1929–1940 (2019).
- W. Xie, T. Komljenovic, J. Huang, M. Tran, M. Davenport, A. Torres, P. Pintus, and J. Bowers, "Heterogeneous silicon photonics sensing for autonomous cars [Invited]," *Opt. Express* **27**, 3642–3663 (2019).
- Y. Wang, G. Zhou, X. Zhang, K. Kwon, P.-A. Blanche, N. Triesault, K.-S. Yu, and M. C. Wu, "2D broadband beamsteering with large-scale MEMS optical phased array," *Optica* **6**, 557–562 (2019).
- S. A. Miller, Y.-C. Chang, C. T. Phare, M. C. Shin, M. Zadka, S. P. Roberts, B. Stern, X. Ji, A. Mohanty, O. A. Jimenez Gordillo, U. D.

- Dave, and M. Lipson, "Large-scale optical phased array using a low-power multi-pass silicon photonic platform," *Optica* **7**, 3–6 (2020).
22. N. Dostart, B. Zhang, A. Khilo, M. Brand, K. Al Qubaisi, D. Onural, D. Feldkhun, K. H. Wagner, and M. A. Popović, "Serpentine optical phased arrays for scalable integrated photonic lidar beam steering," *Optica* **7**, 726–733 (2020).
 23. O. Solgaard, A. A. Godil, R. T. Howe, L. P. Lee, Y. Peter, and H. Zappe, "Optical MEMS: from micromirrors to complex systems," *J. Microelectromech. Syst.* **23**, 517–538 (2014).
 24. B. Smith, B. Hellman, A. Gin, A. Espinoza, and Y. Takashima, "Single chip lidar with discrete beam steering by digital micromirror device," *Opt. Express* **25**, 14732–14745 (2017).
 25. C. Errando-Herranz, N. Le Thomas, and K. B. Gylfason, "Low-power optical beam steering by microelectromechanical waveguide gratings," *Opt. Lett.* **44**, 855–858 (2019).
 26. C. Yousefzadeh, A. Van Rynbach, and P. J. Bos, "Design of a large aperture, tunable, Pancharatnam phase beam steering device," *Opt. Express* **28**, 991–1001 (2020).
 27. J. A. Frantz, J. D. Myers, R. Y. Bekele, C. M. Spillmann, J. Naciri, J. Kolacz, H. G. Gotjen, V. Q. Nguyen, C. C. McClain, L. Brandon Shaw, and J. S. Sanghera, "Chip-based nonmechanical beam steerer in the midwave infrared," *J. Opt. Soc. Am. B* **35**, C29–C37 (2018).
 28. K. Kondo, T. Tatebe, S. Hachuda, H. Abe, F. Koyama, and T. Baba, "Fan-beam steering device using a photonic crystal slow-light waveguide with surface diffraction grating," *Opt. Lett.* **42**, 4990–4993 (2017).
 29. H. Ito, T. Tatebe, H. Abe, and T. Baba, "Wavelength-division multiplexing Si photonic crystal beam steering device for high-throughput parallel sensing," *Opt. Express* **26**, 26145–26155 (2018).
 30. A. Martin, D. Dodane, L. Leviandier, D. Dolfi, A. Naughton, P. O'Brien, T. Spuessens, R. Baets, G. Lepage, P. Verheyen, P. De Heyn, P. Absil, P. Feneyrou, and J. Bourderionnet, "Photonic integrated circuit-based FMCW coherent LiDAR," *J. Lightwave Technol.* **36**, 4640–4645 (2018).
 31. H. Zhou, Y. Zhao, W. Wang, J. Yang, M. Wang, and X. Jiang, "Performance influence of carrier absorption to the Mach-Zehnder-interference based silicon optical switches," *Opt. Express* **17**, 7043–7051 (2009).
 32. D. Sun, Z. Hu, S. Abdul-Majid, R. Vandusen, Q. Zheng, I. Hasan, N. G. Tarr, S. Bidnyk, and T. J. Hall, "Limitation factor analysis for silicon-on-insulator waveguide Mach-Zehnder interference-based electro-optic switch," *J. Lightwave Technol.* **29**, 2592–2600 (2011).
 33. K. Van Acoleyen, W. Bogaerts, J. Jágerská, N. Le Thomas, R. Houdré, and R. Baets, "Off-chip beam steering with a one-dimensional optical phased array on silicon-on-insulator," *Opt. Lett.* **34**, 1477–1479 (2009).
 34. J. Zou, Y. Yu, M. Ye, L. Liu, S. Deng, and X. Zhang, "Ultra efficient silicon nitride grating coupler with bottom grating reflector," *Opt. Express* **23**, 26305–26312 (2015).
 35. Y. Chen, T. Domínguez Bucio, A. Z. Khokhar, M. Banakar, K. Grabska, F. Y. Gardes, R. Halir, Í. Molina-Fernández, P. Cheben, and J.-J. He, "Experimental demonstration of an apodized-imaging chip-fiber grating coupler for Si₃N₄ waveguides," *Opt. Lett.* **42**, 3566–3569 (2017).
 36. W. D. Sacher, Y. Huang, L. Ding, B. J. F. Taylor, H. Jayatilaka, G.-Q. Lo, and J. K. S. Poon, "Wide bandwidth and high coupling efficiency Si₃N₄-on-SOI dual-level grating coupler," *Opt. Express* **22**, 10938–10947 (2014).
 37. C. V. Poulton, M. J. Byrd, P. Russo, E. Timurdogan, M. Khandaker, D. Vermeulen, and M. R. Watts, "Long-range LiDAR and free-space data communication with high-performance optical phased arrays," *IEEE J. Sel. Top. Quantum Electron.* **25**, 7700108 (2019).
 38. F. Aflatouni, B. Abiri, A. Rekhi, and A. Hajimiri, "Nanophotonic coherent imager," *Opt. Express* **23**, 5117–5125 (2015).
 39. C. V. Poulton, A. Yaacobi, D. B. Cole, M. J. Byrd, M. Raval, D. Vermeulen, and M. R. Watts, "Coherent solid-state LiDAR with silicon photonic optical phased arrays," *Opt. Lett.* **42**, 4091–4094 (2017).
 40. R. Fatemi, B. Abiri, A. Khachaturian, and A. Hajimiri, "High sensitivity active flat optics optical phased array receiver with a two-dimensional aperture," *Opt. Express* **26**, 29983–29999 (2018).
 41. C. Rogers, A. Y. Piggott, D. J. Thomson, R. F. Wiser, I. E. Opris, S. A. Fortune, A. J. Compston, A. Gondarenko, F. Meng, X. Chen, G. T. Reed, and R. Nicolaescu, "A universal 3D imaging sensor on a silicon photonics platform," *Nature* **590**, 256–261 (2021).
 42. J. Riemensberger, A. Lukashchuk, M. Karpov, W. Weng, E. Lucas, J. Liu, and T. J. Kippenberg, "Massively parallel coherent laser ranging using a soliton microcomb," *Nature* **581**, 164–170 (2020).
 43. X. Yin, J. Jin, M. Soljačić, C. Peng, and B. Zhen, "Observation of topologically enabled unidirectional guided resonances," *Nature* **580**, 467–471 (2020).
 44. X. Ji, F. A. S. Barbosa, S. P. Roberts, A. Dutt, J. Cardenas, Y. Okawachi, A. Bryant, A. L. Gaeta, and M. Lipson, "Ultra-low-loss on-chip resonators with sub-milliwatt parametric oscillation threshold," *Optica* **4**, 619–624 (2017).
 45. M. H. P. Pfeiffer, J. Liu, A. S. Raja, T. Morais, B. Ghadiani, and T. J. Kippenberg, "Ultra-smooth silicon nitride waveguides based on the Damascene reflow process: fabrication and loss origins," *Optica* **5**, 884–892 (2018).
 46. J. Joo, J. Park, and G. Kim, "Cost-effective 2 × 2 silicon nitride Mach-Zehnder interferometric (MZI) thermo-optic switch," *IEEE Photon. Technol. Lett.* **30**, 740–743 (2018).
 47. B. Bhandari, C. S. Im, K. P. Lee, S. M. Kim, M. C. Oh, and S. S. Lee, "Compact and broadband edge coupler based on multi-stage silicon nitride tapers," *IEEE Photon. J.* **12**, 6602511 (2020).